

Atomistic Mechanisms of Adhesion and Shear Strength in Graphene
Oxide-Polymer Interfaces

Jin Y. Choi , Xu Zhang , Hoang T. Nguyen , Michael R. Roenbeck ,
Lily Mao , Rafael Soler-Crespo , SonBinh T. Nguyen ,
Horacio D. Espinosa

PII: S0022-5096(21)00225-8
DOI: <https://doi.org/10.1016/j.jmps.2021.104578>
Reference: MPS 104578



To appear in: *Journal of the Mechanics and Physics of Solids*

Received date: 8 June 2021
Accepted date: 19 July 2021

Please cite this article as: Jin Y. Choi , Xu Zhang , Hoang T. Nguyen , Michael R. Roenbeck ,
Lily Mao , Rafael Soler-Crespo , SonBinh T. Nguyen , Horacio D. Espinosa , Atomistic Mechanisms
of Adhesion and Shear Strength in Graphene Oxide-Polymer Interfaces, *Journal of the Mechanics and
Physics of Solids* (2021), doi: <https://doi.org/10.1016/j.jmps.2021.104578>

This is a PDF file of an article that has undergone enhancements after acceptance, such as the addition
of a cover page and metadata, and formatting for readability, but it is not yet the definitive version of
record. This version will undergo additional copyediting, typesetting and review before it is published
in its final form, but we are providing this version to give early visibility of the article. Please note that,
during the production process, errors may be discovered which could affect the content, and all legal
disclaimers that apply to the journal pertain.

Atomistic Mechanisms of Adhesion and Shear Strength in Graphene Oxide-Polymer Interfaces

Jin Y. Choi¹, Xu Zhang,¹ Hoang T. Nguyen,¹ Michael R. Roenbeck,^{2,3} Lily Mao⁴, Rafael Soler-Crespo¹, SonBinh T. Nguyen,⁴ Horacio D. Espinosa^{1,2,*}

Affiliations:

¹Theoretical and Applied Mechanics Program, Northwestern University, 2145 Sheridan Rd., Evanston, IL 60208, USA

²Department of Mechanical Engineering, Northwestern University, 2145 Sheridan Rd., Evanston, IL 60208, USA

³Department of Marine Engineering, United States Merchant Marine Academy, 300 Steamboat Road, Kings Point, NY 11024, USA

⁴Department of Chemistry, Northwestern University, 2145 Sheridan Rd., Evanston, IL 60208, USA

*Corresponding author: espinosa@northwestern.edu (H. D. Espinosa)

Abstract

Combining experimental and computational studies of nanocomposite interfaces is highly needed to gain insight into their performance. However, there are very few literature reports, combining well-controlled atomic force microscopy experiments with molecular dynamic simulations, which explore the role of polymer chemistry and assembly on interface adhesion and shear strength. In this work, we investigate graphene oxide (GO)-polymer interfaces prevalent in nanocomposites based on a nacre-like architectures. We examine the interfacial strength resulting from van der Waals and hydrogen bonding interactions by comparing the out-of-plane separation and in-plane shear deformations of GO-polyethylene glycol (PEG) and GO-polyvinyl alcohol (PVA). The investigation reveals an overall better mechanical performance for the anhydrous GO-PVA system

in both out-of-plane and in-plane deformation modes, highlighting the benefits of the donor-acceptor hydrogen bond formation present in GO-PVA. Such bond formation results in inter-chain hydrogen bond networks leading to stronger interfaces. By contrast, PEG, a hydrogen bond acceptor only, relies primarily on van der Waals inter-chain interactions, typically resulting in weaker interactions. The study also predicts that water addition increases the adhesion of GO-PEG but decreases the adhesion of GO-PVA, and slightly increases the shear strength in both systems. Furthermore, by comparing simulations and experiments, we show that the CHARMM force field has enough accuracy to capture the effect of polymer content, water distribution, and to provide quantitative guidance for achieving optimum interfacial properties. Therefore, the study demonstrates an effective methodology, in the Materials Genome spirit, toward the design of 2D materials-polymer nanocomposites system for applications demanding mechanical robustness.

Keywords: graphene oxide, polymer, nanocomposites, adhesion energy, interfacial shear strength; molecular dynamics

1. Introduction

The emergence of graphene-based materials has enabled a fruitful era of research in the design of biological and chemical sensors (Mannoor et al. 2012, Borini et al. 2013), water separation membranes (Hu and Mi 2013), and structural materials (Dikin et al. 2007, Xie et al. 2018). Specifically, graphene oxide (GO), an oxidized variant of graphene, has been combined with a variety of synthetic and biopolymers in fabricating nacre-like nanocomposites for simultaneous enhancement in strength and toughness (Putz et al. 2010, Wan et al. 2016, Wan et al. 2016). In these nanocomposites, a key factor governing their macroscale mechanical behavior is the strength of the GO-polymer interface (Wan et al. 2016). Despite many experimental successes in the past few years, detailed quantitative explorations of the GO-polymer interface and their mechanical response are still scarce (Soler-Crespo et al. 2016, Soler-Crespo et al. 2018). Such scarcity is due to several ongoing challenges, *i.e.*, conducting well-controlled nanoscale experiments and formulating simulation tools capable of reproducing experimental measurements. Overcoming such challenges is critical in paving the way for a guided design of nanocomposites with better mechanical performance as required by new demanding applications in transportation and aerospace exploration.

There are several design variables affecting the strength of GO-polymer interfaces, *e.g.*, polymer type, polymer content, polymer chain length, water content (Compton et al. 2012, Wan et al. 2016, Soler-Crespo et al. 2018, Soler-Crespo et al. 2019, Zhang et al. 2019). From a chemistry perspective, GO possesses a heterogeneous structure comprised of distinct graphitic and oxidized domains (Erickson et al. 2010, Wei et al. 2015, Benedetti et al. 2018, Soler-Crespo et al. 2019). On the graphitic domains, carbon atoms maintain the sp^2 hybridization, thus enabling capabilities to form π - π stacking with the aromatic rings on the backbones or side groups of the adsorbed polymers (Song et al. 2017). In comparison, oxidized domains contain clustered oxygen-containing functional

groups including hydroxyls, epoxides, carbonyls, and carboxyls. They allow the formation of hydrogen bonds (HBs) within themselves, with a second layer of GO, or with the functional groups on the adsorbed polymers. Besides, van der Waals (vdW) interactions exist ubiquitously on both the graphitic and oxidized domains even when pi-pi stacking and HBs are not available. Hydrogen bonding is frequently adopted as the primal interfacial interaction in GO-based nanocomposites due to its relatively strong interaction strength in comparison to other non-bonded interactions. A plethora of HB-capable, synthetic and bio-polymers such as poly(vinyl alcohol) (PVA) (Putz et al. 2010), poly(methyl methacrylate) (PMMA) (Putz et al. 2010) poly(acrylic acid) (Wan et al. 2016), silk fibroin (Xie et al. 2018), and chitosan (Wan et al. 2015) have been combined with GO to form macroscopic nanocomposites with enhanced strength and toughness in comparison to GO paper. Inspired by the finding that GO can be significantly toughened, via polymer crack bridging (Soler-Crespo et al. 2019), Espinosa and co-workers utilized molecular dynamics (MD) simulations to explore the capability of these polymers, as an ultra-thin polymer adlayer, to hinder the crack propagation of GO through crack-bridging (Zhang et al. 2019). By exploring a library of oxygen-containing polymers, they revealed that vdW interactions, generally considered a weak type of interaction, can also provide significant interfacial strength leading to the enhanced fracture toughness of monolayer GO. The role of chemistry and bond-type suggests promising strategies to expand the range of polymers to be used in the design and fabrication of GO-polymer based nanocomposites with superior mechanical performance beyond those exhibiting HB-forming chemistries. In support of this conclusion, Owuor et al. showed that GO-polydimethylsiloxane (PDMS) nanocomposites, in which PDMS interacts with GO primarily through vdW interactions, exhibit enhanced toughness in comparison to GO foam ($28 \times$ higher toughness with 1.5 wt% of polydimethylsiloxane) (Owuor et al. 2017). However, a more comprehensive experimental investigation of the simulated library of polymers is needed.

Herein, we report a systematic nanomechanical experimental/computational exploration on the strength of the two aforementioned interfacial interactions—hydrogen bonding and vdW interactions. Specifically, GO-polyvinyl alcohol (PVA) and GO-polyethylene glycol (PEG) material systems were selected and studied due to the stronger HB-donor and acceptor capability of PVA *versus* the more pronounced vdW interactions of PEG (Zhang et al. 2019). Unlike the previous computational study, the strength of the interface was characterized by interfacial separation (out-of-plane) and shear (in-plane) through both atomic force microscopy (AFM) experiments and molecular dynamics (MD) simulations. Also, the composite is arranged in a layered architecture inspired by nacre and the intercalated polymer content is varied in MD to study the effect of interchain HBs. We show that by performing well-controlled experiments and selecting accurate MD force fields, good agreement between experiments and simulations is obtained. The study reveals the advantages of polymer chains in strengthening the GO-GO interactions, over smaller molecules, *e.g.*, water (Soler-Crespo et al. 2018). Indeed, the adsorbed PVA chains provide an overall stronger interface in an anhydrous system due to their extensive hydrogen bonding network with GO and between themselves. Interestingly, addition of water to the GO-polymer systems results in interface adhesion strengthening (GO-PEG) and weakening (GO-PVA) effects.

The combined experimental-computational study lays a foundation for exploring a large family of 2D materials-polymer nanocomposites, that when augmented with AI algorithms, should lead to accelerated development of multifunctional materials.

2. Methods

2.1. Sample Preparation

GO was synthesized by the modified Hummers method following the protocols established in a previous work (Soler-Crespo et al. 2018). For substrates, a piece of a clean silicon wafer with

285 nm SiO_2 thickness was cut with a diamond scribe and sonicated in acetone and isopropyl alcohol for 20 minutes each. The wafer was then rinsed with deionized water, blown dry with compressed air, and treated with oxygen plasma. For AFM tips, SiO_2 spheres ~6 micron in diameter, stored in ethanol solution, were deposited onto the wafer and viewed in Nova NanoSEM 600. Optimal spheres without visible roughness (at 30,000x magnification, 5 kV, 0.45 nA) were selected and mapped. Spherical tips were then assembled to cantilevers in an optical microscope probe station. No-tip AFM cantilevers (NANOSENSORS™, TL-FM model) were sputter-coated on the back side with reflective metallic coating and attached to a custom-designed arm extending from a micromanipulator. Cantilevers were then dipped into a small bead of fast-drying epoxy and, subsequently, used to pick up the preferred sphere.

The as-synthesized GO sheets were first transferred onto the as-treated substrate via the LB technique (Soler-Crespo et al. 2018, Cote, 2009 #15). A thin and smooth layer of PEG was then achieved by slowly dipping and withdrawing the GO-coated substrates from a PEG solution, following the Langmuir-Blodgett protocols. GO-PVA samples were prepared by spin-coating PVA solution onto the GO-coated substrates. To create the GO-polymer interface (see Fig. 1a), GO sheets were transferred onto the spherical SiO_2 AFM tip via dip-coating. The locations of GO flakes and polymer patches on the SiO_2 substrates were checked with optical microscopy, while the presence of GO on spheres was confirmed by Raman spectra obtained before testing (Soler-Crespo et al. 2018).

Substrates were placed in sealed containers, prior to testing, for at least several hours to guarantee a stable moisture equilibrium. Relative humidity (RH) during AFM experiments was controlled at two levels: dry (16-20% relative humidity) and humid (40-45% relative humidity). In each case, polymer “regions” formed on the substrates due to the presence of a sacrificial tape

marker (on spin-coated PVA) or meniscus effects from solution adhesion (in the case of PEG deposited by the LB technique). In both cases, polymer layers have a thickness of approximately 5 nanometers as measured by AFM scans aligned transversely to these regions. In addition, within line scans over areas corresponding closely to the expected contact region ($\sim 100 \text{ nm} \times 100 \text{ nm}$), the surface roughness of each polymer was measured to be ~ 0.15 nanometers, closely matching the measured roughness of GO sheets on the same substrates. The similarity between the surface roughness values of all tested substrates is important for minimizing potential variations in separation and shear measurements that could arise from topological, rather than material, differences.

2.2. AFM Adhesion and Shear Experiments

Out-of-plane separation and in-plane shear are two fundamental deformation modes at GO-polymer interfaces. In multilayer GO-polymer nanocomposites, these two deformation modes are activated under various loading conditions; separation takes place in tension along the stacking directions, while shear occurs during motion perpendicular to the stacking plane. To probe the adhesive properties of these interfaces, we performed indentation tests using the AFM technique (Fig. 1a). Before testing, a large GO flake with polymer was found on the substrate and scanned in tapping mode. Then, the GO-coated spherical cantilever was brought into contact with one part of the flake. The cantilever was extended until positive deflections of $\sim 40 \text{ nm}$ were observed (corresponding to compressive interactions with the substrate) and then retracted. In all tests, a sudden pull-out event was observed. This pull-out displacement was converted into a force $F_{pullout}$ using the normal cantilever stiffness, (Cannara et al. 2006) *i.e.*,

$$F_{pullout} = \frac{k_{norm} \Delta V_{norm}}{s_{norm} \cos \theta}, \quad (1)$$

where s_{norm} is the cantilever normal sensitivity, ΔV_{norm} is the voltage signals, and θ is the angle at pull-off with respect to the horizontal direction. To investigate the repeatability of these measurements, at least 5 tests were performed at 5 different locations (*i.e.*, no part of the GO flake was subjected to two independent tests).

In shear experiments, the frictional force F_f was varied as a function of the normal force F_n , with each component given by,

$$F_f = \frac{k_{lat}}{s_{lat}} \left(\frac{\Delta V_{lat}}{2} \right) \quad (2)$$

$$F_n = \frac{k_{norm}}{\cos \theta s_{norm}} \Delta V_{norm} \quad (3)$$

where k , s , and ΔV correspond to the stiffness, sensitivity, and voltage signals in the lateral and normal modes as indicated by the subscripts (see Appendix A for stiffness and sensitivity determinations for both separation and shear deformation modes).

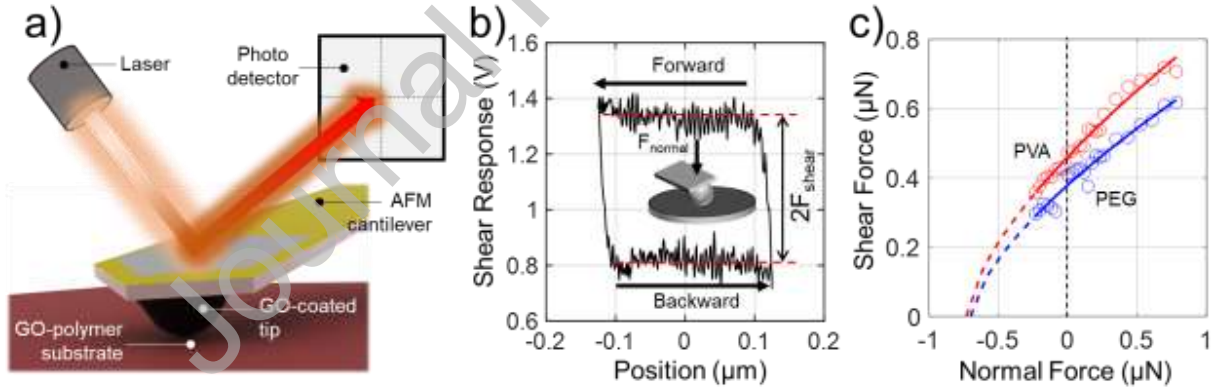


Fig. 1. (a) Schematic of the experimental AFM setup in which a GO-coated AFM tip contacts the GO-polymer-coated substrate, measuring interfacial response from separation and shear (frictional) motions. (b) A representative measurement of the shear load voltage for a given applied normal load (F_{norm}). (c) Shear-Force-Normal Force experimental data and fit to extract interfacial properties.

The approach utilized in this study primarily relies upon the test probe method previously developed by Cannara *et al.* (Cannara et al. 2006). An in-depth description is given in Appendix A. Measured values of F_f and F_n were fitted against a contact theory by Derjaguin, Muller, and Toporov (DMT-theory) (Derjaguin et al. 1975). This theory differs from Hertzian contact by an “offset” for adhesion energy present outside the contact zone, which is widely adopted for contacts between hard elastic solids and weak, long-range adhesive interactions. DMT theory is shown to be a good approximation to interactions in the current systems, (see Fig. 1c) and can be summarized as:

$$F_f = F_0 \left(1 - \frac{F_n}{F_{pullout,DMT}} \right)^{\frac{2}{3}} \quad (4)$$

From fitting the interaction coefficient, shear strength at zero normal force and adhesive energy are extracted, the later cross-validated with the value measured in the pull-off tests mentioned above. In addition, the relation between contact radius and applied load is predicted by

$$a_0 = \left(\frac{2\pi GR^2}{K} \right)^{\frac{1}{3}} \quad (5)$$

where the effective stiffness is given by

$$K = \frac{4}{3} \left(\frac{1-\nu_1^2}{E_1} + \frac{1-\nu_2^2}{E_2} \right)^{-1} \quad (6)$$

Note that the DMT-theory implies that there is no contact area at the interface at the point of separation, but this occurs at a non-zero normal load equal to

$$G = \frac{F_{pullout,DMT}}{-2\pi R} \quad (7)$$

where G is the adhesion energy across the interface, calculated from Eqn. (7), and R is the radius of the indenter. Even though DMT theory is appropriate for this study, it is worth mentioning that other contact theories should be used for other contact scenarios, *e.g.*, Johnson, Kendall, Roberts

(JKR) (Johnson et al. 1971) or Maugis-Dugdale (via Carpick's data analysis framework) (Carpick et al. 1999).

2.3. Roughness characterization

Surface roughness was measured on top of each sphere using tapping mode AFM scans (Park model XE-120) with sharp Si tips (Bruker TESPA, radius < 12 nm). Root-mean-squared (RMS) roughness was calculated over regions of 100 nm × 100 nm. The curvature of the sphere was subtracted from RMS roughness calculations using second-order fitting across the slow scan direction. Contact interactions are not associated with the entire surface but, rather, can be calculated as the contact interactions between the indenter of radius R with a spherical asperity of radius r . Long-range, non-contact interactions between the indenter and surface are reduced, as the indenter is separated from the mid-plane of the surface by the amplitude of the sinusoid, y_{max} . Therefore, the corrected experimental adhesion is defined as

$$G = \left| \frac{F_{pullout}}{2\pi R} \right| \left[\frac{1}{1 + \frac{32Rk_1R_{q,min}}{\lambda_s^2}} + \frac{1}{\left(1 + \frac{k_1R_{q,min}}{z_0}\right)^2} \right] / \left[\frac{1}{1 + \frac{32Rk_1R_q}{\lambda_s^2}} + \frac{1}{\left(1 + \frac{k_1R_q}{z_0}\right)^2} \right] \quad (8)$$

where, R_q is the RMS surface roughness and λ_s is the mean surface wavelength. k_l is a constant (1.817) associated with close-packed asperities and z_0 is the minimum distance that can be achieved between two continuum surfaces at the atomistic scale. This estimation is appropriate for “shallow” sinusoidal surfaces (*i.e.* with wavelengths much larger than those that would be associated with hemispherical asperities ($\lambda_s = 4r$). It should also be noted that this model is subjected to the constraints $14.5R_q \ll \lambda_s \ll \sqrt{32k_1R_qR}$ (Rabinovich et al. 2000). While the lower bound ensures that the surface wavelength is much larger than the RMS surface roughness, the upper bound ensures that r remains much less than R . It should be noted that this correction is not applied to the shear strength, τ . While shear and adhesion are closely related, literature reports have not applied

such a correction before, as the mechanisms which govern shear behavior are markedly different. Therefore, the interfacial shear strength is reported as in DMT model without any modification.

2.4. Molecular Dynamic Simulations

2.4.1. Model Configuration

To explore differences in molecular interactions of the two polymers with GO, as well as between polymer chains, we conducted MD computations on GO-PVA and GO-PEG systems and simulated the interfacial separation and shear motions explored experimentally. To be consistent with the tested material systems, we created an epoxide-rich GO (4:1 epoxide/hydroxyl ratio) possessing heterogeneous structures with distinct graphitic and oxidized domains according to high resolution transmission electron microscope imaging as reported in (Soler-Crespo et al. 2019) (Fig. 2). The polymer chains were generated using an in-house random walk-based algorithm. For both polymers, 134 monomers (DP=134) were used corresponding to a 6kDa molecular weight (measured experimentally). The polymer chains and patchy GO were combined into a single data file. We studied various polymer adsorption scenarios ranging from preferable adsorption onto the oxidized regions of GO to the formation of a continuous layer on GO. Those systems correspond to 4, 8, and 15 polymer chains on a $10 \times 10 \text{ nm}^2$ GO sheet, respectively.

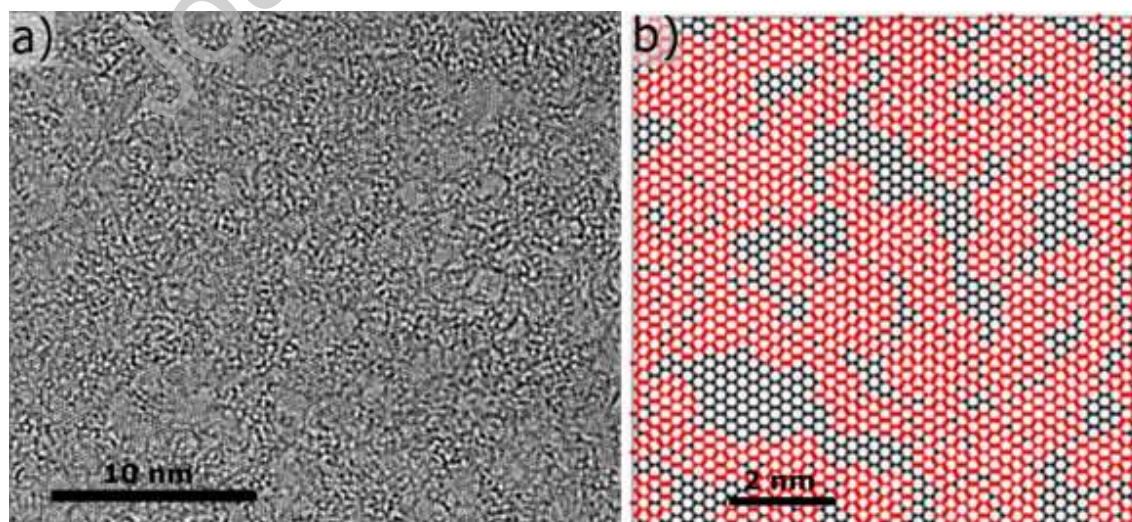


Fig. 2. (a) An HRTEM image of a GO sheet showing graphitic islands interspersed in oxidized domains (b) Top-down view of the generated GO structure used for simulations. The oxidized regions are shown in red, and the graphitic regions are shown in black.

2.4.2. Equilibration of Simulated System

The Large-scale Atomic/Molecular Massively Parallel Simulator (LAMMPS) (Plimpton 1995) was used to conduct the MD simulations. Periodic boundary conditions were used in all directions, and the height of the simulation box was set to 15 nm to prevent interaction between periodic boundaries in the z-direction. The CHARMM general force field (CGenFF) (Vanommeslaeghe et al. 2010) was used to model the selected GO-polymer systems. CGenFF program (interface version 1.0.0, force field version 3.0.1) (Vanommeslaeghe et al. 2012) was used to obtain the atomic charges and force field parameters for bonded interactions of polymer molecules. The Lennard-Jones parameters for polymers were obtained from CGenFF C36 version (Vanommeslaeghe et al. 2010, Yu et al. 2012), and the force field parameters for GO were taken from Fonseca et al. (Fonseca et al. 2016). The assembly was performed under the NVT ensemble with the number of molecules, system volume, and temperature of the system constant. First, a “soft” potential was used to spread the polymer chains, and a repulsive potential wall was used to push the polymer chains toward GO to facilitate the contact. Afterwards, the potential wall was removed and the full CHARMM potential was deployed to let the polymer naturally adhere to the GO. The entire system was equilibrated at 650K for 6ns, then the temperature was slowly lowered to 300K over the next 1.5 ns to anneal the polymer. The final annealed structures were equilibrated under the NVE and NPT ensembles for 72 ps to create a GO intergallery filled with the adsorbed polymer layers as the starting point for interfacial separation and shear simulations.

Water molecules were introduced in selected GO-PVA and GO-PEG simulations to explore the effect of water, which cannot be completely eliminated in experiments due to relative humidity and associated AFM tip-substrate meniscus formation. The GO-polymer-water system was initially

assembled in the same way as the GO-polymer system, except that 260 water molecules (~10 wt% with respect to the polymer layer) were added through the use of a solvation box, see Visual Molecular Dynamics (VMD) (Humphrey et al. 1996). We noticed that water molecules were not evenly distributed. Hence, to overcome this issue, an additional annealing step (650K for 6ns, lowered to 300K for 1.5ns) was added after the NPT ensemble. The systems prepared by both methods, referred to as “unannealed” and “annealed” system (see Appendix B), respectively, were simulated in both interfacial separation and shear.

2.4.3 Interfacial Separation and Shear Simulations

In the interfacial separation simulations, a total separation of 30 nm was prescribed by increasing the size of the simulation box, over a 2.4 ns of simulation time, along the out-of-plane direction, i.e., by enlarging the GO intergallery spacing. This corresponds to a separation rate of 12.5 m/s or strain rates ranging between 1.19×10^{10} /s to 4.7×10^9 /s depending on the thickness of the polymer. For interfacial shear simulations, an in-plane shear strain was applied to a triclinic box to simulate the shearing of adjacent layers, for a total of 10 nm of interfacial sliding over a simulation time of 0.6 ns, which corresponds to a sliding rate of 16.7 m/s or a shear strain rate ranging between 1.59×10^{10} /s to 6.28×10^9 /s depending on the polymer content. The deformation velocities for the separation and shear simulations are comparable to rates that exhibited converging results in previous studies (Soler-Crespo et al. 2019, Zhang et al. 2019). Nonetheless, the effects of strain rate was explored by simulating the 8-polymer systems at 10x, 0.1x, 0.01x rates in shear and was fitted to a hierarchical Bell’s model previously used in MD studies of proteins with hydrogen bonding (Ackbarow et al. 2007). The Bell’s model is ultimately fit to an equation of the form,

$$f = a \ln(v) + b \quad (9)$$

where a and b are constants containing information of the bond breaking chemistry and v is the deformation velocity. The details of the derivation and the terms can be found in Ackbarow et al. While the fit was obtained for 8-PEG and 8-PVA shear MD, the identified Bell's model was applied to correct for rate effects in other polymer contents as well as the out-of-plane simulations. The traction displacement for different rates and the Bell's model fit can be found in Appendix C.

All MD simulations were performed at 300 K. During the interfacial separation and shear simulations, stresses corresponding to the specific deformation mode were recorded for subsequent analysis. Radius of gyration was also computed during the simulations. HBs of various types were counted using an in-house code. The visualization of the system was accomplished with OVITO (Stukowski 2009).

3. Results and Discussion

3.1. GO-Polymer Interfaces at Equilibrium

An equilibrated GO-PVA system, prior to any deformation, is depicted in Fig. 3. For clarity, only two of the polymer chains are represented, which span across the periodic box giving the appearance of multiple polymer chains. The intergallery polymer layer increases the interlayer spacing of GO (*e.g.*, from 0.56 nm with 4 PVA chains to 1.44 nm with 15 PVA chains) and hence it weakens direct GO-GO interactions. However, the flexibility of polymer chains enables favorable interfacial interactions beyond the local rigidity of GO sheets, resulting in a stronger interfacial strength (Putz et al. 2010). A distinct difference between PVA and PEG is the formation of HBs: PVA chains can both accept/donate hydrogen atoms from/to GO, the same chain, and another PVA chain. In contrast, PEG is only capable of accepting hydrogen atoms from the hydroxyl groups present on GO. Regardless of differences in chemistry, interfacial vdW interactions exist for both polymers. However, its contribution in PEG is more prominent due to the same number of atoms in

the monomer of both polymers but a smaller distance from PEG's backbone (where the majority of the vdW interactions arises from) to the GO surface.

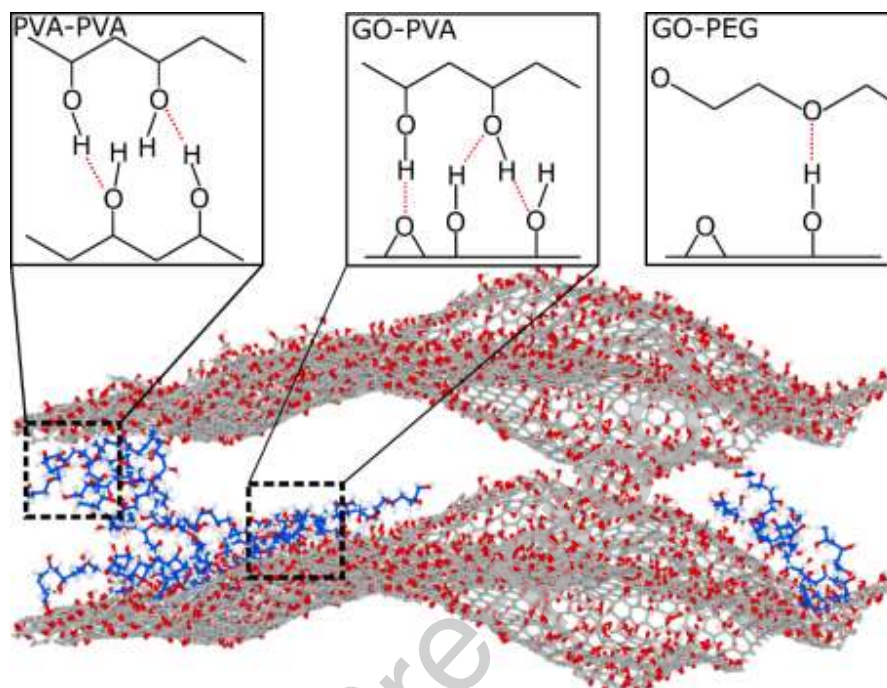


Fig. 3. An overview of 15 PVA chain system after equilibration. The carbon atoms on graphene are shown in gray and are shown in blue on the PVA backbone. The oxygen atoms are shown in red, and hydrogen atom are shown in white. 13 of 15 chains have been omitted in the visualization for clarity. The zoom-in illustrates various HBs including PVA-PVA interchain H-bond (left), GO-PVA (middle) and GO-PEG (right).

3.2. Interface Adhesion – Comparison between MD Simulations and Experiments

The normal traction along the separation direction, plotted against the separation distance, is shown in Fig. 4a. The normal traction sharply increases to its peak value and quickly tapers off as the layers are separated further. Notably, the normal traction can be maintained up to 30 and 45 nm, which corresponds to the contour length of the PVA and PEG chains studied herein. Such a long bridging distance is in sharp contrast to the behavior of GO-GO and GO-water-GO systems, under the same type of interfacial separation where the normal traction vanishes after 3 nm (Soler-Crespo et al. 2018). This highlights the advantage of employing extensible polymer chains, over small molecules, for resisting interfacial separation.

While the peak traction decreases, as the number of chains increase (see Appendix D), the total adhesion energy, calculated by integrating the normal traction-separation curve (Fig. 4a), increases with the number of polymer chains (Fig. 4b). The MD adhesion energy predictions are consistently larger than experimental values but stay within the same order of magnitude. The discrepancy could be attributed to the strain rate effect. Even though we apply the hierarchical Bell's model to mitigate such effect, the lowest strain rate we could use with confidence for such a fit ($10^8/s$) was not as low as the experimental strain rate as discussed in Appendix C. In addition, water may be present in experiments despite the low humidity conditions, which is explored through GO-polymer-water MD simulations, as discussed below.

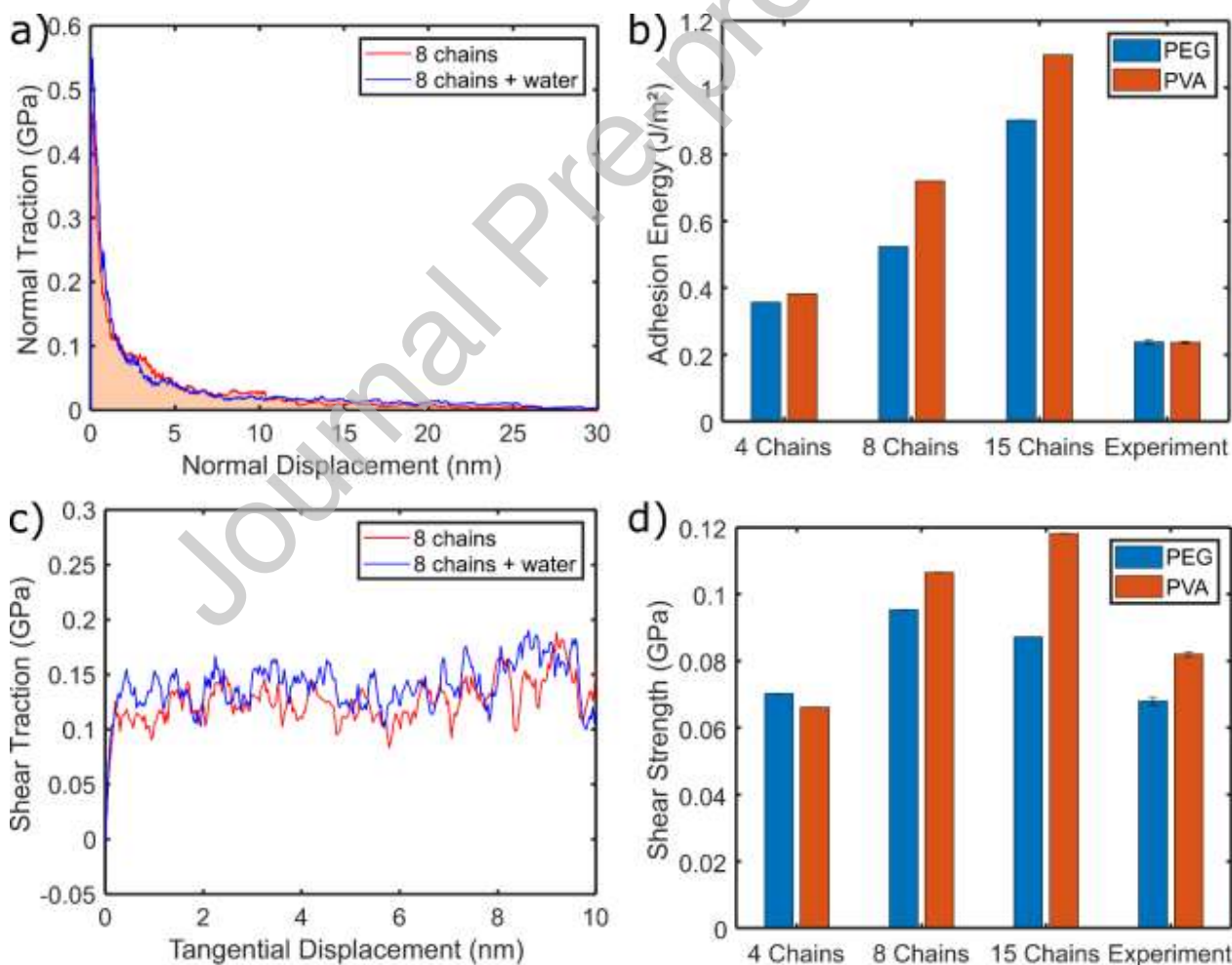


Fig. 4. (a) A representative normal traction-normal displacement curve obtained from the interfacial separation simulation for a GO-PVA system with 8 PVA chains with and without water. The integration of this curve, as represented by the shaded region, provides the adhesion energy. (b) Adhesion energies obtained from simulations of the GO-polymer systems with 4, 8, 15 polymer chains (no water) and comparison to experimental measurements (RH 16-20%). (c) A representative shear traction-tangential displacement curve obtained from the shear simulation the GO-PVA system with 8 PVA chains with and without water. The dashed line represents the region where the shear stress was averaged. (d) Shear traction obtained from simulations of the GO-polymer systems with 4, 8, and 15 polymer chains (no water) and comparison to experimental measurements (RH 16-20%).

Interestingly, the adhesion energy of the GO-PEG and GO-PVA systems is almost identical in experiments (RH 16-20%, see Appendix G). In contrast, MD simulations predict similar adhesion energy for the 4-chain system and larger values for the GO-PVA system with increasing number of chains. The GO-PVA adhesion energies were higher than for GO-PEG by 38% and 22% for 8 and 15 chains, respectively. In an anhydrous system, such trend can be explained by the system-dependent relative contribution from the GO-polymer and polymer-polymer interactions. With fewer chains, the adhesion energy mainly originates from GO-polymer interactions through all the monomers that are closely-adsorbed onto the GO surface. The equal adhesion energy observed for the 4-chain system, arises from i) the same per-monomer binding energy for PVA and PEG when adsorbed on GO (Zhang et al. 2019), and ii) no constraints in space for the monomers to interact with GO. As the number of chains increases, contributions from the polymer-polymer interactions increase and the HB network between PVA chains further enhances the interfacial adhesion, resulting in higher adhesion energy.

In the presence of water, the simulated adhesion energy of GO-PVA and GO-PEG becomes similar consistent with the experimental measurements, see Fig. 5a. Water increases adhesion in PEG and decreases adhesion in PVA. While the predicted adhesion energy is higher than the one measured experimentally, for the reasons previously discussed, the qualitative interface response is in good agreement. In previous work, we reported that water plays a significant role in mediating interfacial properties between GO flakes (Soler-Crespo et al. 2018), and its role seems to extend to

GO-polymer interfaces as well. Indeed, the addition of water results in large prediction variations, specifically in the adhesion strength of PVA, due to the distribution of water in the system: locally congregated water molecules significantly decrease the adhesion energy of GO-PVA while well-distributed water molecules enhance the adhesion energy (see Appendix B). This dual strengthening/weakening effect of water arises from different equilibration conditions and is only observed in the GO-PVA system. The GO-polymer-water simulation reported in Fig. 5 is an average of the two distinct scenarios, which may exist in experiments (see Appendix B). The combined experimental and simulation results suggest comparable adhesion energy for the GO-PVA and GO-PEG systems.

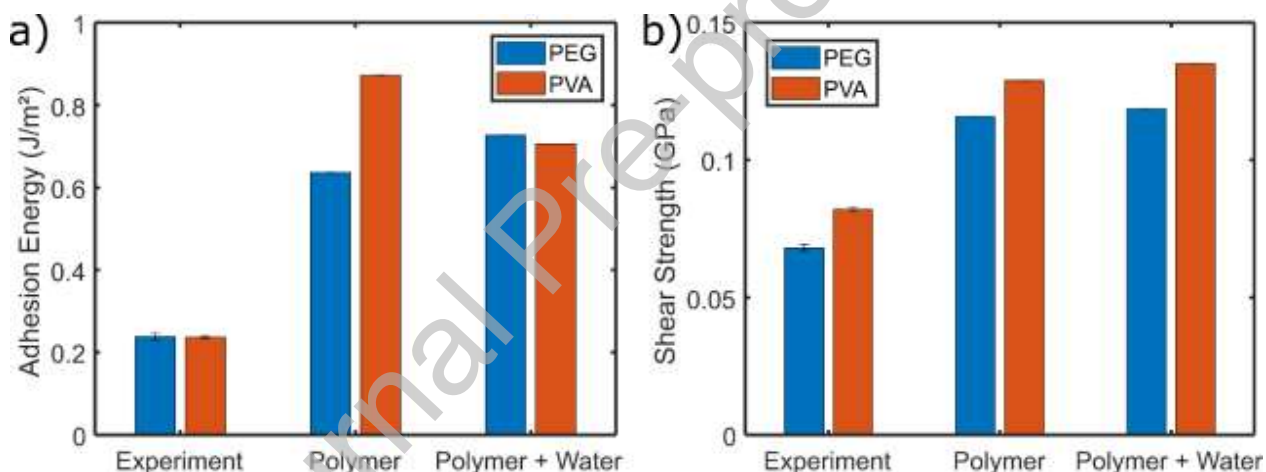


Fig. 5. Comparison of experimental and MD simulations for the (a) adhesion energy and (b) shear strength with and without water. Here, the simulation results are not scaled using the Bell's model as the strain rate effect was not fitted for the hydrated system. The GO-polymer-water system is an average of two separate runs with different degrees of equilibration (further explained in Appendix B.).

To explore and quantify the configurational change of polymer chains during separation, we computed the radius of gyration for each chain throughout the separation process. The average radius of gyration, for the GO-PVA systems (Fig. 6a), reflects sequential detachment of polymer chains from the GO surface: it increases as the polymer chains bridging the GO layers are stretched out and drops suddenly due to detachment and snap-back of the bridging polymer chains onto either

of the GO surfaces. When the PVA chains snap back onto the GO, they either adhere onto the unsaturated GO surface or the existing PVA layer, indicated by the radius of gyration values returning to almost initial values by the end of simulation. For the GO-PEG systems, the same phenomena are observed but the radius of gyration at the end of the run, is higher than its initial value due to incomplete separation, whose early termination had negligible contribution to the adhesion energy (see Appendix E).

Fig. 6b-d show various snapshots for the GO-PVA and GO-PEG systems during the interfacial separation (see Supporting Information, Movie 1-3 for full movies of the interfacial separation process), which capture distinct polymer configurations as the GO layers are separated. The polymer can just stay on one side of the GO without bridging, form a linear bridge, a U-shaped bridge, an interconnected network (*i.e.*, polymers bridging with the aid of other polymers), and a mix of all the aforementioned modes. As the polymer count increases, they tend to form more interconnected networks and bundled structures which can contribute to the increase in adhesion energy through polymer-polymer interactions. The measured traction (Fig. 4a) is generated by all the polymer bridges at the GO interface, which actively transfer load and inhibit the separation.

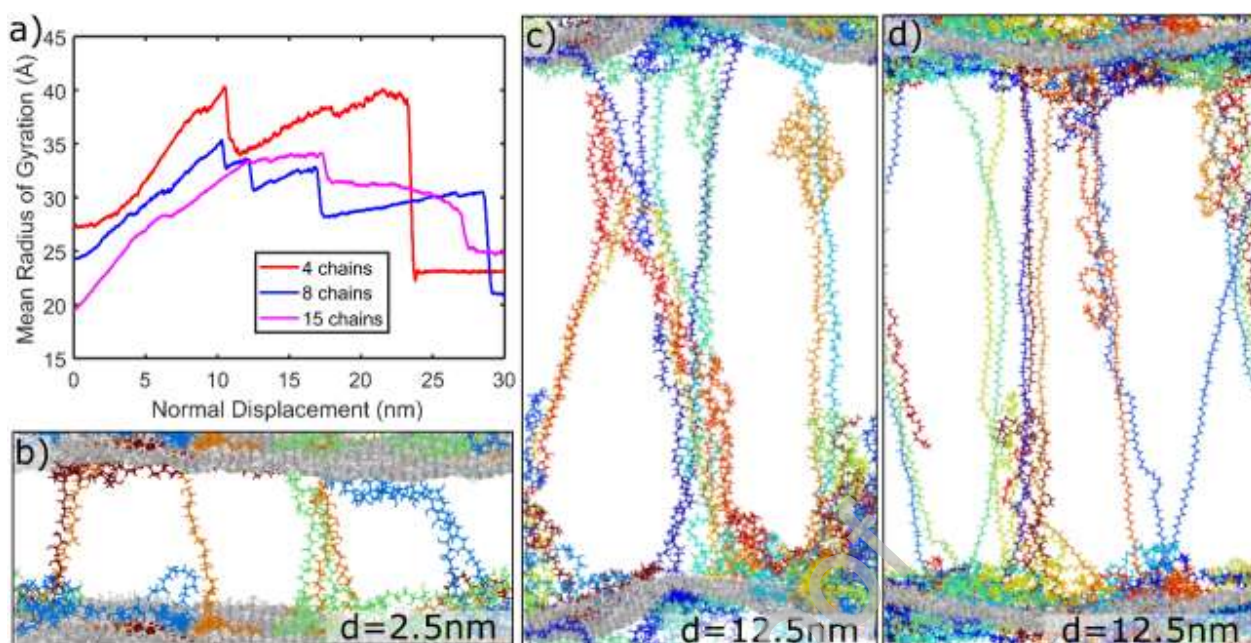


Fig. 6. (a) Average radius of gyration for PVA chains during adhesion simulations. Simulation snapshots during out-of-plane separation (b) 4 PVA chains at $d=3\text{nm}$, (c) 15 PVA chains at $d=12.5\text{nm}$ (d) 15 PEG chains at $d=12.5\text{nm}$

The difference between PVA and PEG, with regard to their interactions with GO, is further explored with an analysis on HBs and interfacial interaction energies. We counted the number of hydrogen bonds in the GO-polymer systems with the following criterion: donor-acceptor distance $< 3.5 \text{ \AA}$ and H-acceptor-donor angle $< 30^\circ$ (Luzar and Chandler 1996). As observed in Fig. 7a-c, PVA chains form much more HBs with GO than PEG chains. Furthermore, PVA forms PVA-PVA interchain HBs while PEG cannot form HBs with other PEG chains. As the neighboring GO layers are separated, the GO-PVA HBs decrease due to detachment of chain segments from the GO surface. However, even after the PVA chains break off and adhere back onto either GO surface, the GO-PVA HB numbers are not fully restored to pre-separation numbers. This is due to the clustering of PVA chains as in the case of 15 PVA chains, which is further supported by an increase of the PVA-PVA interchain HBs for the 15-chain system.

Notably, the adhesion energy does not scale with the number of HBs in the system: on an average basis, the number of GO-PVA HBs is 20 times in comparison to that of GO-PEG, but its adhesion energy is only 22% higher on average. This inconsistency points out to the limitation of using the number of HBs as a quantitative measurement of the interfacial strength: at a given separation, HBs of polymer chains that do not bridge the GO-GO interface, both directly and indirectly, do not contribute to load transfer but are still counted. More importantly, the contributions from vdW are not reflected in the number of HBs. To understand the relative contribution between hydrogen bonding and vdW interactions, we decomposed the (change of) interfacial energy between GO and the polymer layer into percentage contributions from the two components that describe those two types of interactions in MD simulations, namely, Coulombic and Lennard-Jones (LJ), respectively (Sinko and Keten 2015, Zhang et al. 2019). As shown in Fig. 7d, GO-PVA systems have consistently higher Coulombic contributions to the energy than their GO-PEG counterpart systems with the same number of chains. For GO-PEG systems, vdW interactions contribute ~70% to the interaction energies in comparison to hydrogen bonding, indicating significant roles of vdW interactions in strengthening the interface. For GO-PVA systems, the contribution from vdW interactions is relatively smaller (~62%) but is still higher than Coulombic interactions. Such behavior can be explained by the competing roles of PVA-PVA and PVA-GO hydrogen bonding in limiting the PVA chains to achieve maximum HB forming capacity with GO.

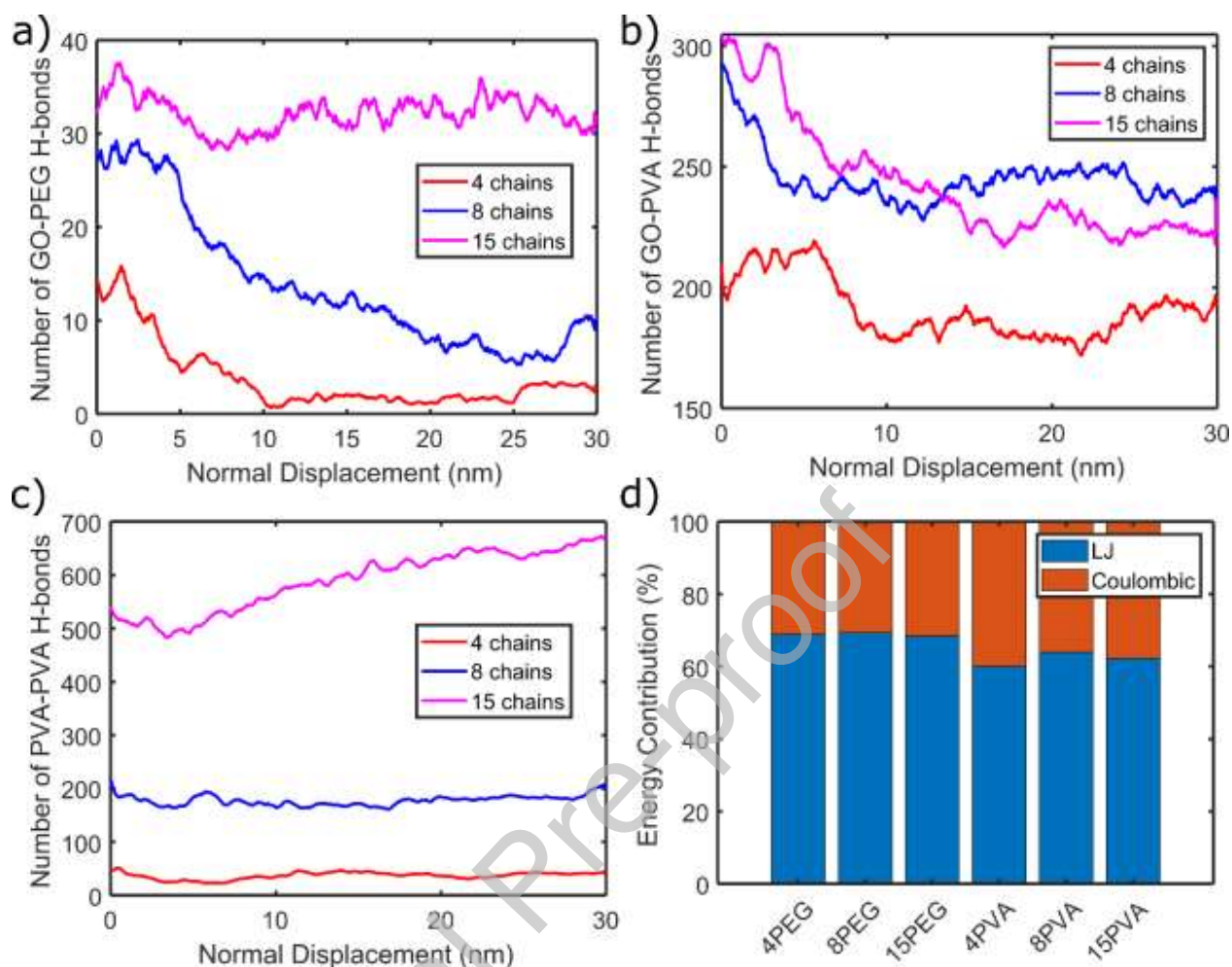


Fig. 7. (a-c) Change of PVA-PVA, GO-PVA, and GO-PEG HBs throughout interfacial separation, respectively. HBs were counted with the following criterion: donor-acceptor distance < 3.5 Å and H-acceptor-donor angle $< 30^\circ$ (Luzar and Chandler 1996). (d) Normalized GO-polymer energy decomposition into Lennard-Jones (LJ) and Coulombic interactions as a function of polymer and number of chains. The two energy terms reflect vdW and hydrogen-bonding interactions, respectively.

3.3 Interface Shearing - Comparison between MD Simulations and Experiments

The interfacial shear simulations were configured with the same initial configurations as the interfacial separation simulations but the simulation box was sheared in the in-plane direction, causing the GO sheet and its periodic image to slide across in the in-plane direction (see Fig. 8b-d). We measured the interfacial shear traction corresponding to the shearing direction and plotted it as a function of the shearing displacement (see Fig. 4c for the GO-8-PVA-chain system, and Fig. C.1 for

the rest of the systems). The shear traction-tangential displacement shows local peak-and-valley patterns, indicative of stick-slip motions at the interface, which were also observed in GO-GO (Soler-Crespo et al. 2018), GO-water (Soler-Crespo et al. 2018), and GO-polymer (Zhang et al. 2019) systems. The mean interfacial shear stress was calculated after 2.5 nm of displacement to capture the dynamic steady-state shear behavior, and the results are summarized in Fig. 4d. As the number of chains increases, the average shear traction increases and saturates/decreases starting from the 8-chain systems, where full coverage on GO is achieved. Interestingly, the saturation of average shear traction is more obvious in comparison to the adhesion energies (Fig. 4b). Such different response to the increase of polymer content indicates distinct interaction mechanisms for the two motions: in interfacial separation, increased polymer chains provide more flexibility in strengthening the interface through various bridging scenarios (direct and indirect bridges, the formation of polymer bundles, etc.); in interfacial shear, such flexibility is largely limited due to much more localized interactions. Thus, the effect of increasing polymer content has diminishing returns in increasing the interfacial shear strength.

For all the simulated systems, except for the 4 polymer chain systems in which the GO interactions dominate, GO-PVA possesses higher average shear stress in comparison to GO-PEG, consistent with experimental observations (Fig. 4d). In simulations, the GO-PVA shear strength were higher than GO-PEG by 12%, 36% for 8 and 15 chains, respectively, and 21% higher for GO-PVA in experiment. Qualitatively, such trend agrees with our previous study, in which a short PVA (DP = 40) chain showed higher average resisting force per monomer in comparison to a PEG (DP = 27) chain as both chains are pulled off from the GO surface (Zhang et al. 2019). With the addition of water molecules, the “unannealed” system (Appendix B) with more aggregated water molecules led to a small decrease of 1.6% and 2.8% in the shear strength for PVA and PEG, respectively. The “annealed” system with more evenly distributed water led to an increase in shear strength of 5.4%

and 6.5% for both PVA and PEG, respectively. While the effects are relatively small, the water distribution affects the shear strength of both polymers similarly.

Following the same approach as for the interfacial separation systems, we measured the average radius of gyration for the polymer chains during the interfacial separation (Fig. 8a) and for visualization purpose, highlighted two chains of the GO-15-PVA-chain system (Fig. 8b-d). The polymer chains simply tilt, like a deck of cards, with respect to the adjacent GO layers. Adhesion to its initial GO positions is preserved, with small increase in the radius of gyration (Fig. 8a). Unlike water (Soler-Crespo et al. 2018), the polymer chain is long enough to elongate with the GO as the two layers are sheared, and only begin to peel-off the initial GO position once sufficient shear displacement is applied.

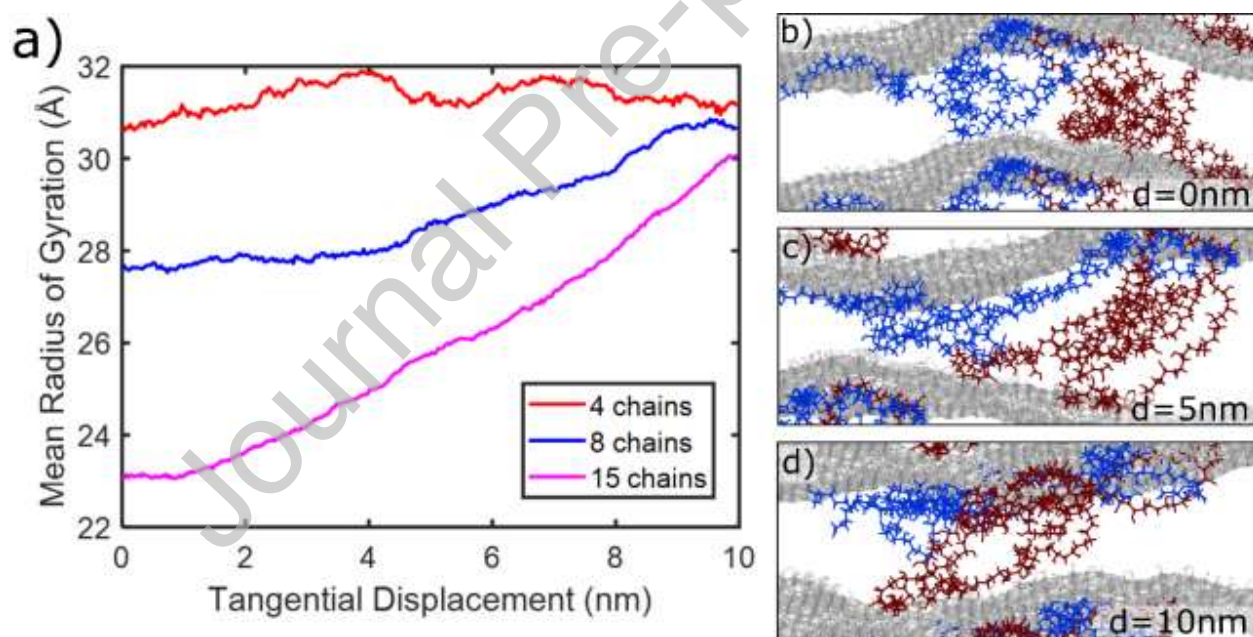


Fig. 8. (a) Average radius of gyration change during interfacial shear for GO-PVA systems. The increase of radius of gyration is smaller in comparison to interfacial separation simulations, indicating more localized motions of polymer chains. (b-d) Simulation snapshots during interfacial shear for 15 PVA chains (13 of the 15 polymer chains are omitted for clarity of visualization). PVA chains tilt and align until one of the chains (blue one) peels off as the GO is sheared.

The evolution of HBs for PVA-PVA, GO-PVA, and GO-PEG is illustrated in Fig. 9. The PVA-PVA inter-chain HBs increase slightly as the system is subjected to shear while the GO-PVA HBs decrease, indicating favorable conditions for inter-chain HBs to form as PVA chains are elongated and aligned during shear. As for the GO-PVA HBs, the decrease arises from detachment of PVA monomers from the GO. For PEG, the HBs slightly fluctuate with no obvious trend. Since the interfacial shear and separation simulations have the same initial configuration, the energy decomposition (Fig. 7d) remains consistent for interfacial shear simulations, with higher vdW contributions for GO-PEG systems.

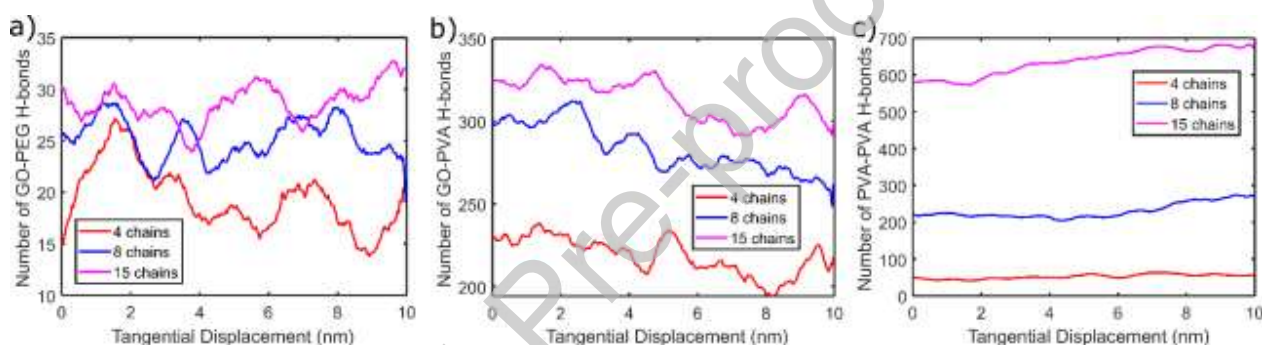


Fig. 9. (a-c) Change of HBs during interfacial shear simulations for PVA-PVA, GO-PVA and GO-PEG systems.

3.4 Implications on Material Design

Our results strongly advocate the effect of polymer adlayer in strengthening the intergallery interface between GO sheets. The rigid carbon backbones act as strong bridging media between re-formable interfacial HBs and vdW clusters, thus maintaining the integrity of the interface over a large range of deformation. Such strengthening effects, at a larger scale, should significantly enhance the mechanical performance (strength, toughness etc.) of the composites in comparison to pure GO films, as has been demonstrated in various GO-polymer systems (Putz et al. 2010, Wan et al. 2016, Wang et al. 2016).

If a monolayer of reinforcing polymer is desired (*e.g.*, an atomically-thin layer of polymer fabricated with the Langmuir-Blodgett deposition) (Soler-Crespo et al. 2019), polymers with limited hydrogen bonding capability should provide equal interfacial strengthening in comparison to those with better hydrogen bonding capability. We ascribe such a trend to the significant contribution from the vdW interactions in maintaining interfacial integrity. The advantage of strong hydrogen bonding capability emerges upon the formation of an extensive HB network in systems with larger polymer content, allowing better load-transfer and reinforcing effect.

The tradeoff between interfacial strength and composite stiffness needs to be balanced by identifying the optimum polymer content, as revealed by this work and demonstrated experimentally for chitosan (Wan et al. 2015) and PAA (Wan et al. 2016) in fabricating graphene-based composites. For adhesion, increasing the polymer content linearly increases the adhesion energy but at the cost of decreasing stiffness as shown in Fig. 10a. An optimum can be found by plotting the sum of the squared of the normalized parameters that does not compromise either (see Appendix F). This corresponds to 9.2 polymer chains for PEG (polymer/GO 81wt%), and 10.2 polymer chains for PVA (polymer/GO 89wt%). At this polymer content, the shear strength also shows an optimal value where it starts to saturate without additional benefit from increased polymer, as shown in Fig. 10b.

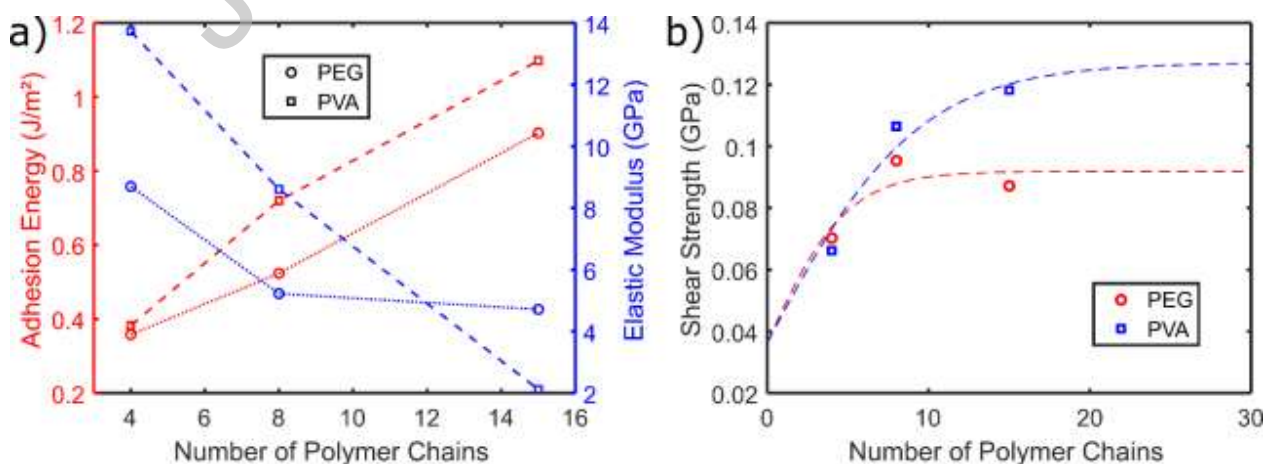


Fig. 10. (a) Tradeoff of adhesion energy and elastic modulus (b) nonlinear hyperbolic tangent fit showing the plateauing of the shear strength with increasing polymer

We notice a dual effect of water as both a strengthening and lubricating media in tuning the interfacial mechanical response in hydrogen bonding-dominated GO-polymer systems. Such a finding indicates an optimum water content level for interfacial strengthening, which has been demonstrated in graphene oxide paper (Compton et al. 2012) and graphene oxide-PVA nanocomposites (Medhekar et al. 2010). In contrast, the optimum water content level appears larger in a hydrogen-bonding-limited GO-polymer system due to its more dominant “short-ranged” bridging effect that indirectly improves the hydrogen bonding interactions between GO and polymer. We thus anticipate that such hydrogen-bonding-limited systems possess better mechanical integrity in applications at high-humidity levels, *e.g.*, water separation membranes (Hu and Mi 2013).

4. Concluding Remarks

We investigated the difference between vdW and hydrogen-bonding interactions in modulating interfacial interactions in GO-polymer nanocomposites. PEG and PVA were selected to highlight the vdW and hydrogen bonding interactions at the GO-polymer interface, respectively. The strength of the interface was characterized by interfacial separation (out-of-plane) and shear (in-plane) deformation in AFM-based experiments and MD simulations. In both experiments and simulations, we identified a strong strengthening effect from polymer chains due to their stretchability. MD simulations reveal that either polymer can provide a similar interfacial strengthening effect if a monolayer of reinforcing polymer is employed. Thicker polymer layers exhibit superior adhesion and shear but at the cost of decreased interfacial stiffness. In the case of thicker polymer layers, the nature of the bond formation is important and by adopting polymers with high HB-forming capability stiffness and toughness can be optimized. A dual strengthening/weakening effect of water is identified in the GO-PVA interface, which suggests the

necessity to optimize water content in GO-polymer nanocomposite systems. As a polymer with limited HB-forming capability, PEG still possesses comparable adhesion energy and slightly lower shear strength in comparison to PVA, thus highlighting the potential of deploying vdW interactions in strengthening a wide range of materials systems that do not possess hydrogen bonding capabilities.

We show that an overall good agreement between experiments and MD simulations can be achieved with well-controlled experimental configurations and suitable force fields, which in turns enables mechanistic understanding of 2D material-polymer interfaces. As such, the combined experimental-computational methodology here presented provides a roadmap for the investigation of 2D-polymer interfaces including those based on protein fibrils such as collagen, amyloids, *etc.* Moreover, experimentally validated MD simulations offer the opportunity to explore material libraries, in the materials genome spirit, that when combined with AI algorithms could lead to significant speed up in nanocomposite design for specific multifunctionalities.

Acknowledgements

The authors acknowledge the support of the National Science Foundation, through award CMMI 1953806, the Army Research Lab, through award W911NF1220022, and computational resources provided by the Quest High Performance Computing Cluster at Northwestern University. We thank W. Gao for helpful suggestions on the simulations.

Supporting Information

The Supporting Information includes the following items:

- Movie 1. MD simulation of 4-PVA chains in adhesion
- Movie 2. MD simulation of 15-PVA chains in adhesion
- Movie 3. MD simulation of 15-PEG chains in adhesion

- Movie 4. MD simulation of 8-PVA chains in shear
- Movie 5. MD simulation of 8-PEG chains in shear

Journal Pre-proof

Appendix A. Normal and Lateral sensitivity and stiffness calibration

Normal sensitivity and stiffness calibration

The measurement of sample stiffness and normal force/displacement requires the use of a cantilever of known stiffness, whose calibration follows a two-step procedure: sensitivity measurement and stiffness calibration. In the former step, the AFM hardware measures the cantilever deflection in raw units of volts. Thus, a conversion factor, S , relates the raw cantilever deflection as measured by the AFM photodetector (ΔV_c , volts) to the more meaningful absolute cantilever deflection (δ_c , meter), i.e:

$$\delta_c = S \Delta V_c \quad (\text{A.1})$$

S is determined by pressing the AFM cantilever against a rigid sample while the AFM hardware outputs the raw cantilever deflection ΔV_c versus the piezo deflection δ_p . Because the substrate used in calibration is rigid, its deflection is zero, i.e., $\delta_c = \delta_p$. Hence, taking the slope of the ΔV_c vs δ_p plot gives $1/S$ in units of V/m (or S in m/V).

The stiffness calibration, on the other hand, is done by a reference cantilever with defined stiffness, k_s . These precisely manufactured cantilevers can be purchased in a range of well-defined stiffness. The AFM cantilever is pressed against the reference cantilever by extending the z-piezo a distance δ_p as before. This again results in a set of data consisting of the cantilever deflection (ΔV_c , in raw units of volts) versus piezo deflection (δ_p , in units of meters). However, the deflection of the reference cantilever is no longer zero, or $\delta_s \neq 0$. The slope between the raw cantilever deflection and the piezo extension is then calculated:

$$k_{norm} = k_s \left(\frac{S_{ref}}{S_{norm}} - 1 \right) \quad (\text{A.2})$$

Note that S_{ref} and S_{norm} are normal sensitivity of reference and experimental cantilever calibrated by the same method mentioned previously.

Lateral sensitivity and stiffness calibration

Similar to normal stiffness, the calibration of lateral cantilever stiffness also consists of two steps. However, while the technique is straightforward for calibrating the factors in normal direction, a measurement of lateral stiffness is more complicated. First, the lateral sensitivity of the position-sensitive detector (PSD) should be calibrated using the test probe method developed by Cannara et al. (Cannara et al. 2006). In this method, an AFM cantilever with a large attached microsphere is brought into contact with a vertical sidewall (*i.e.* edge) along the substrate, which is displaced over a known distance. As the sidewall pushes the microsphere, variations in lateral voltage signals vs. distance, termed $s_{lat,test}$, are measured. Based on the results obtained from this test probe, as well as other factors (*e.g.* probe geometry and material properties), the lateral sensitivity corresponding to an experimental probe of a different geometry, s_{lat} , can also be obtained. The governing equation developed by Cannara et al. (Cannara et al. 2006) is:

$$s_{lat} = s_{lat,test} \frac{\frac{T}{T_{test}}(1+\varepsilon_{test})}{\frac{h}{h_{test}(1+\varepsilon)}} \quad (A.3)$$

where T is the signal intensity, h is the moment arm, and ε is a bending correction term described in further detail below. For the test probe, the moment arm can be more accurately estimated as the distance from the centroid to the base of the trapezoid plus half the sphere diameter. This is appropriate because the probe is expected to make contact with the vertical wall at the location corresponding to its maximum width, *i.e.* in the center instead of at the base. Here, both h and h_{test} are consequently calculated from SEM image measurements. Here, “*test*” subscripts correspond to parameters of the test probe, while those without subscripts correspond to the probe used in experiments. Cannara et al. (Cannara et al. 2006) computed the signal ratio T/T_{test} by considering the independently measured normal stiffness and normal sensitivity of each cantilever. Using these parameters, it can be shown that:

$$\frac{T}{T_{test}} = \frac{S_{norm}L}{S_{norm,test}L_{test}} \quad (A.4)$$

Where L denotes the length of the cantilever, measured up to the tip. Eq. (A.4) takes into account the fact that, for both the experimental and test probes, the total deflection measured by the PSD is, in fact, the sum of contributions from cantilever twist (corresponding to lateral displacements acting through moment arm h) and in-plane bending. Consequently, the effective stiffness from these two contributions can be treated as springs in series. Cannara et al. (Cannara et al. 2006) denoted the ratio between these terms as ε , *i.e.* $\varepsilon = k_{lat}/k_{ipb}$ where k_{lat} was the (total) lateral stiffness and k_{ipb} was the in-plane bending stiffness. While the latter term cannot be directly measured in experiments, we utilize the normal stiffness of each cantilever (directly measured in experiments) and calculate the in-plane bending stiffness by measuring the geometry of relevant parameters in SEM. The relevant area moments of inertia and in-plane bending stiffness are:

$$I_{ipb} = 1/48t(a+b)(a^2 + b^2) \quad (A.5)$$

$$I_{norm} = \frac{t^3(a^2 + 4ab + b^2)}{36(a+b)} \quad (A.6)$$

$$k_{ipb} = k_{norm} \frac{I_{ipb}}{I_{norm}} \quad (A.7)$$

The lateral stiffness contributed by torsion:

$$k_{tor} = k_{norm} \frac{2L^2}{3(1+\nu)} \quad (A.8)$$

The lateral stiffness k_{lat} can thus be computed:

$$k_{lat} = \left(\frac{1}{k_{ipb}} + \frac{h^2}{k_{tor}} \right)^{-1} \quad (A.9)$$

Where ν is the Poisson's ratio of silicon (0.25). Unlike the test probe, the moment arm in the experiment is taken as the sum of the sphere diameter and the vertical distance to the centroid of the trapezoidal cross section because the contact occurs at the bottom of the sphere, *i.e.*

$$h = 2R + \frac{t(b+2a)}{3(a+b)} \quad (A.10)$$

Where R is the sphere radius, t is the average cantilever thickness, and a and b are the average widths of the top and bottom faces of the trapezoid, respectively. We note that, each of the geometrical parameters is taken from the average of multiple measurements from SEM images.

Unlike the normal force/displacement measurement, the complete lateral stiffness of the cantilever-substrate system in experiments cannot be taken from its beam properties alone. Instead, the total stiffness is a combination of the cantilever, contact, tip, and glue stiffness, *i.e.*

$$\frac{1}{k_{lat,tot}} = \frac{1}{k_{lat}} + \frac{1}{k_{lat,contact}} + \frac{1}{k_{lat,tip}} + \frac{1}{k_{lat,glue}} \quad (\text{A.11})$$

In many cases, the last two terms are considered negligible. Analytical estimates of the contact stiffness suggest that this term must be incorporated here. The contact stiffness is defined as:

$$k_{lat,contact} = 8a \left(\frac{2-\nu_1}{G_1} + \frac{2-\nu_2}{G_2} \right)^{-1} \quad (\text{A.12})$$

It must be noted that, since contact stiffness is directly proportional to the contact radius a , this term is not a constant in shear experiments in which the applied load is varied. Rather, it must be iteratively solved for during the contact analysis.

Appendix B. GO-polymer-water simulations and water distribution analysis

The system was initially prepared in the same methodology as the GO-polymer system without water for consistency. However, we discovered that this led to a disproportionate amount of water congregating at one of the GO interfaces, resulting in a drastic loss of adhesion energy in GO-PVA-water system compared to its GO-PVA counterpart. The simulations show the PVA chains detaching from the locally congregated water molecules, unable to contribute to the adhesion through bridging as observed before in the GO-polymer system.

Further annealing of the same system results in a better distribution of water, better bridging by the polymer, and an increase of the adhesion energy. For clarity, these systems are referred to as

“unannealed” and “annealed” system in Fig. B.1. Interestingly, the effect of water distribution did not affect PEG as much as it did for PVA. This could be due to the fact that the difference between the unannealed and annealed system for PEG in water distribution was not as large as it was for PVA (Fig. B.1, c-d), and/or due to steric effects of having the HB-forming oxygen in the backbone (PEG) versus having a hydroxyl as a branch (PVA) which may interfere with HB formation between polymer and water. Another observation is that the water in the PVA system gravitated towards the GO and avoid being in the center of the polymer, while the water was more evenly distributed in the PEG system, further emphasizing the difference in affinity between the water and the two polymers.

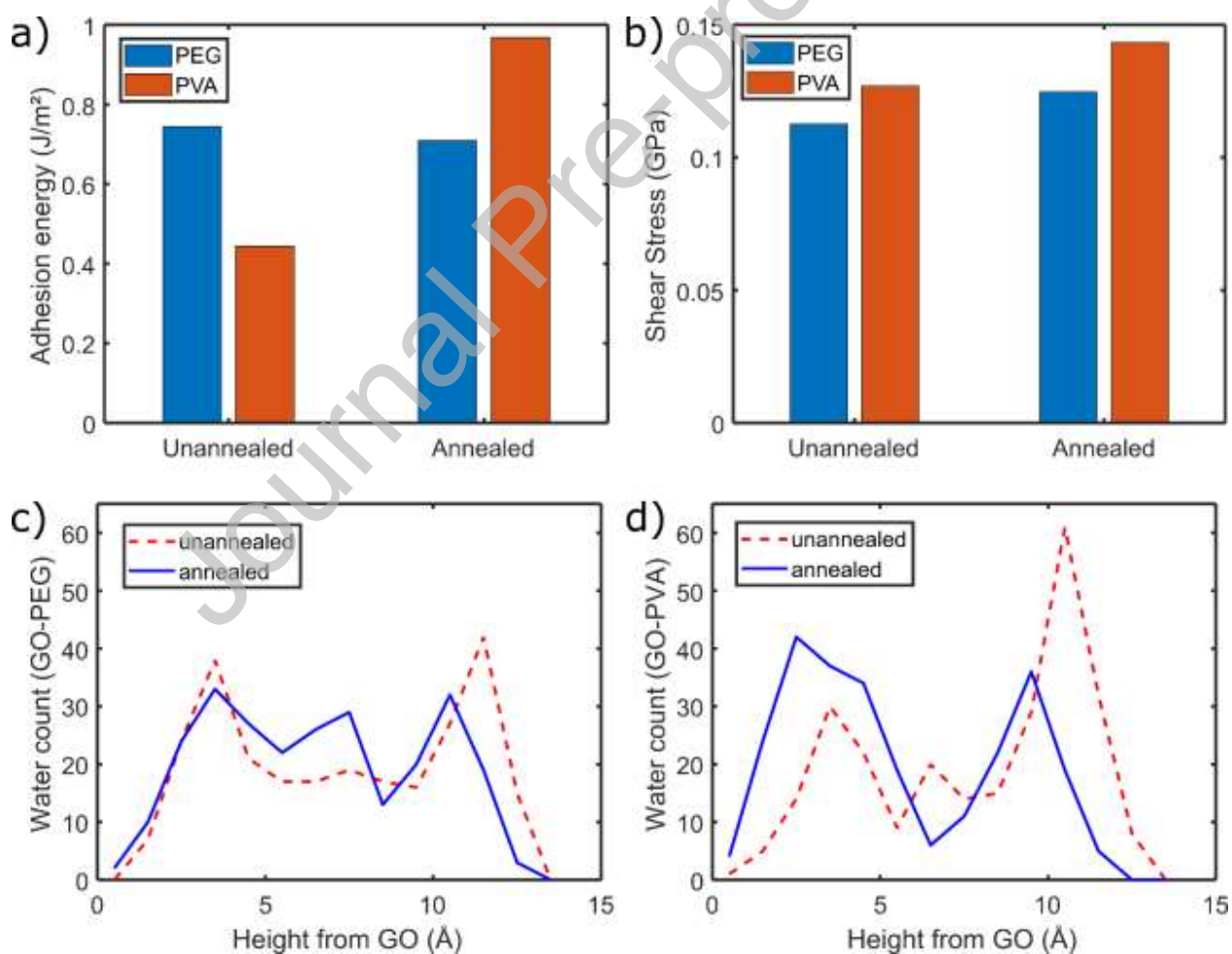


Fig. B.1. (a-b) Comparison of adhesion energies and shear stress obtained from MD simulations of GO-polymer-water systems with and without additional annealing (c-d) line profiles of the number of water molecules as a function of their height from GO surface in (c) GO-PEG and (d) GO-PVA system.

Appendix C. Strain rate effect and hierarchical Bell's model fit

The hierarchical Bell's model is used to account for strain rate effects in MD simulations. The Bell's model consists of two different regimes referred to as the fast deformation mode (FDM) in which HBs break sequentially and the slow deformation mode (SDM) in which few HBs break concurrently (Ackbarow et al. 2007). An approximate fit for the SDM is made with a single experimental point and the slowest MD rate tested, under the assumption that slowest MD rate is on the transition between the two regimes. The lack of data points and the transition point assumption means that the SDM fit cannot be used to scale down MD results to experimental rates. Therefore, the MD results are scaled only within the FDM region and normalized to strain rates of $10^8/\text{s}$. While this does not entirely account for the strain rate difference between the simulation and experiment, it does partially close the gap by scaling within the high slope of the FDM region. Figure C.1 shows the representative traction-displacement curves and the corresponding Bell's model fit.

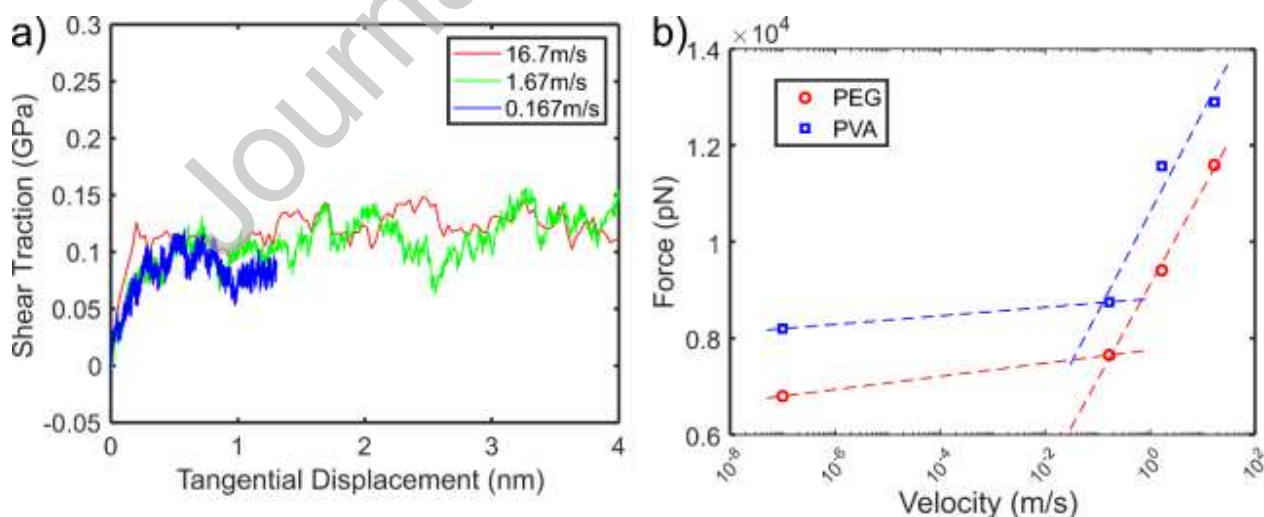


Fig. C.1 a) 8-PVA shear MD traction-displacement plot at different shear rates b) Bell model fit of 8-polymer chain MD shear simulations (3 points on the right), plotted with experimental result (single

point on the left). The dotted lines represent the fitted curves for the slow and fast deformation modes.

Appendix D. Traction-displacement curves for all GO-polymer simulations

Fig. C.1 shows the stress-displacement curves for all the simulations. As mentioned, the peak stress decreases in the adhesion simulations as the number of chains increase. In shear, peaks can be observed for the 4 chain systems near the beginning and end of the simulation. Both are caused by the GO-GO interactions (one GO and its periodic image) due to the proximity of the GOs with only 4 polymer chains, which is why the effect is lessened with more polymers to increase the gap.

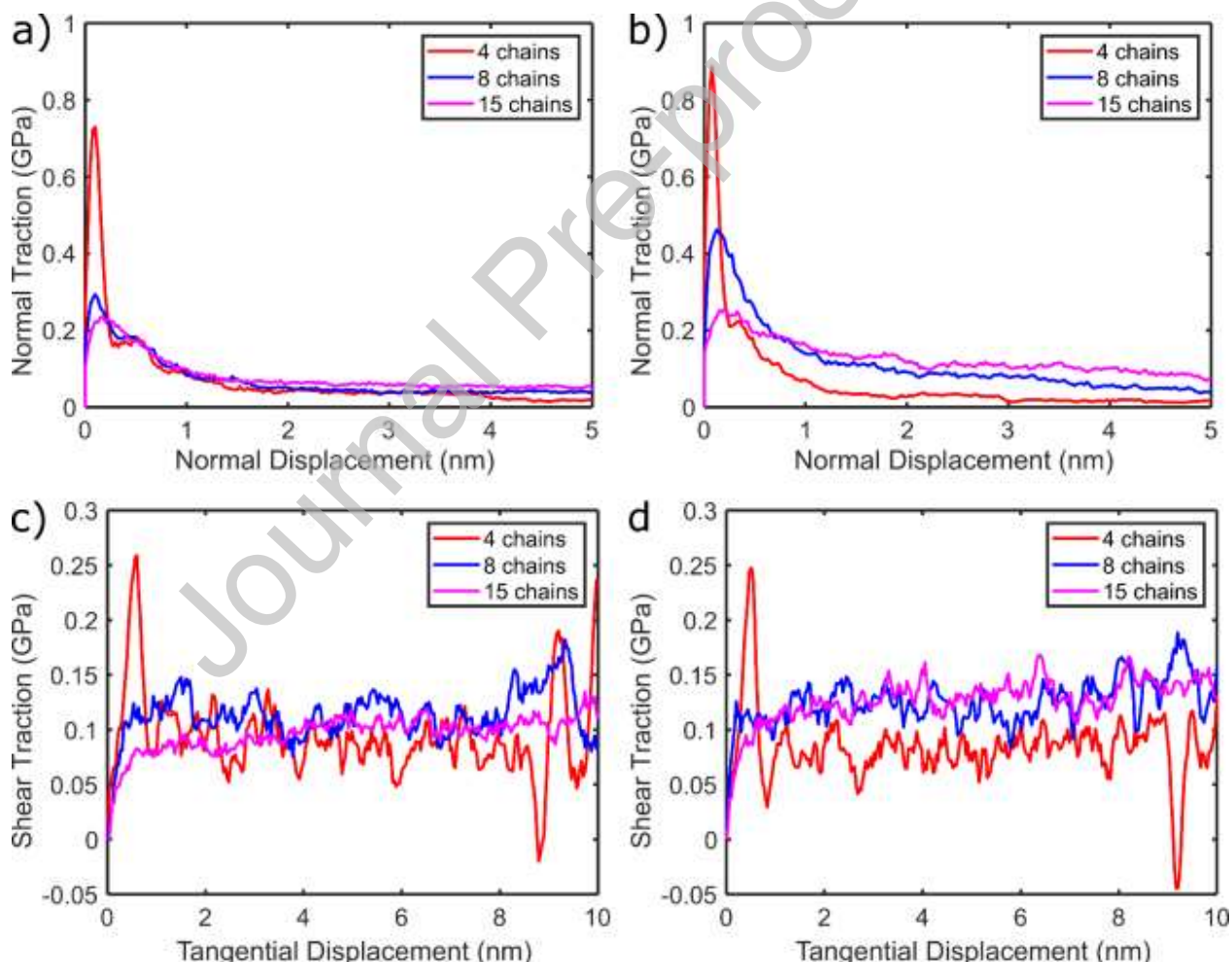


Fig. D.1. Stress-separation curve of (a) all the PEG systems and (b) all the PVA systems in interfacial separation simulations. For (a-b), only 5nm out of 30nm of separation is shown to highlight the

regions of interest at early stages of deformation. (c-d) Stress-displacement curve for (c) all PEG systems and (d) all PVA systems in interfacial shear simulations

Appendix E. Radius of gyration for GO-PEG simulations

Fig. D.1 shows the change in radius of gyration for the PEG simulations. Due to the longer contour length of PEG than PVA, 30nm of separation was enough to detach most of the chains but not all, resulting in the higher radius of gyration than PVA at the end of the run. In shear, the initial radius of gyration indicates that with more polymer, they chains will configure themselves into a more spherical structure initially but stretches as it is sheared, as shown by the converging radius values by the end of the simulation.

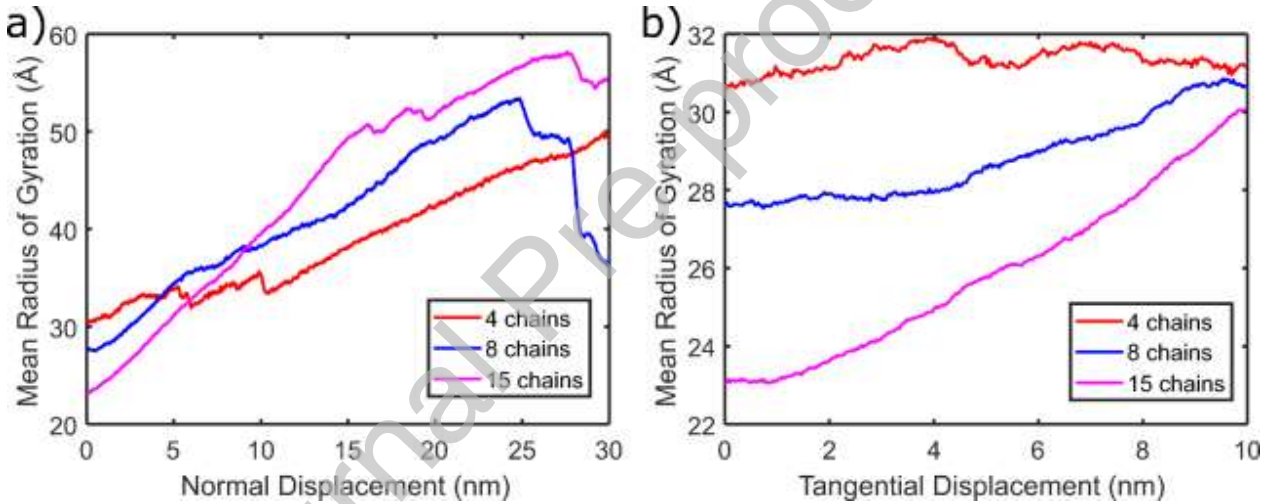


Fig. E.1. The average radius of gyration for all PEG systems in (a) adhesion simulations and (b) in shear simulations.

Appendix F. Optimal polymer content analysis

Because of the tradeoff between the adhesion energy and the out-of-plane stiffness, an optimal polymer content was estimated by plotting the sum of squared normalized stiffness and adhesion energy.

$$S = \left(\frac{E}{E_{Ref}} \right)^2 + \left(\frac{J}{J_{Ref}} \right)^2 \quad (E.1)$$

The reference stiffness and adhesion energy were taken from the largest of each set, which was 4 polymer chain results for stiffness and 15 polymer chain results for adhesion energy. This ensured that the largest value from each squared term would be equal to 1. The minimum is at a balanced point that does not compromise either parameter, and a simple parabolic fit was applied as shown in Fig. E.1. The minima were found at 9.2 chains for PEG (polymer/GO 80.6 wt%), and 10.2 chains for PVA (polymer/GO 89.3 wt%).

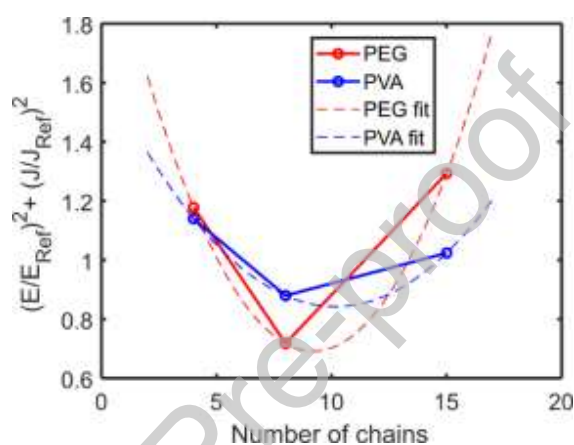


Fig. F.1. Parabolic fit applied to the sum of squared normalized stiffness and adhesion energy.

Appendix G. Experimental interfacial properties at 16-20% and 40-45% relative humidity

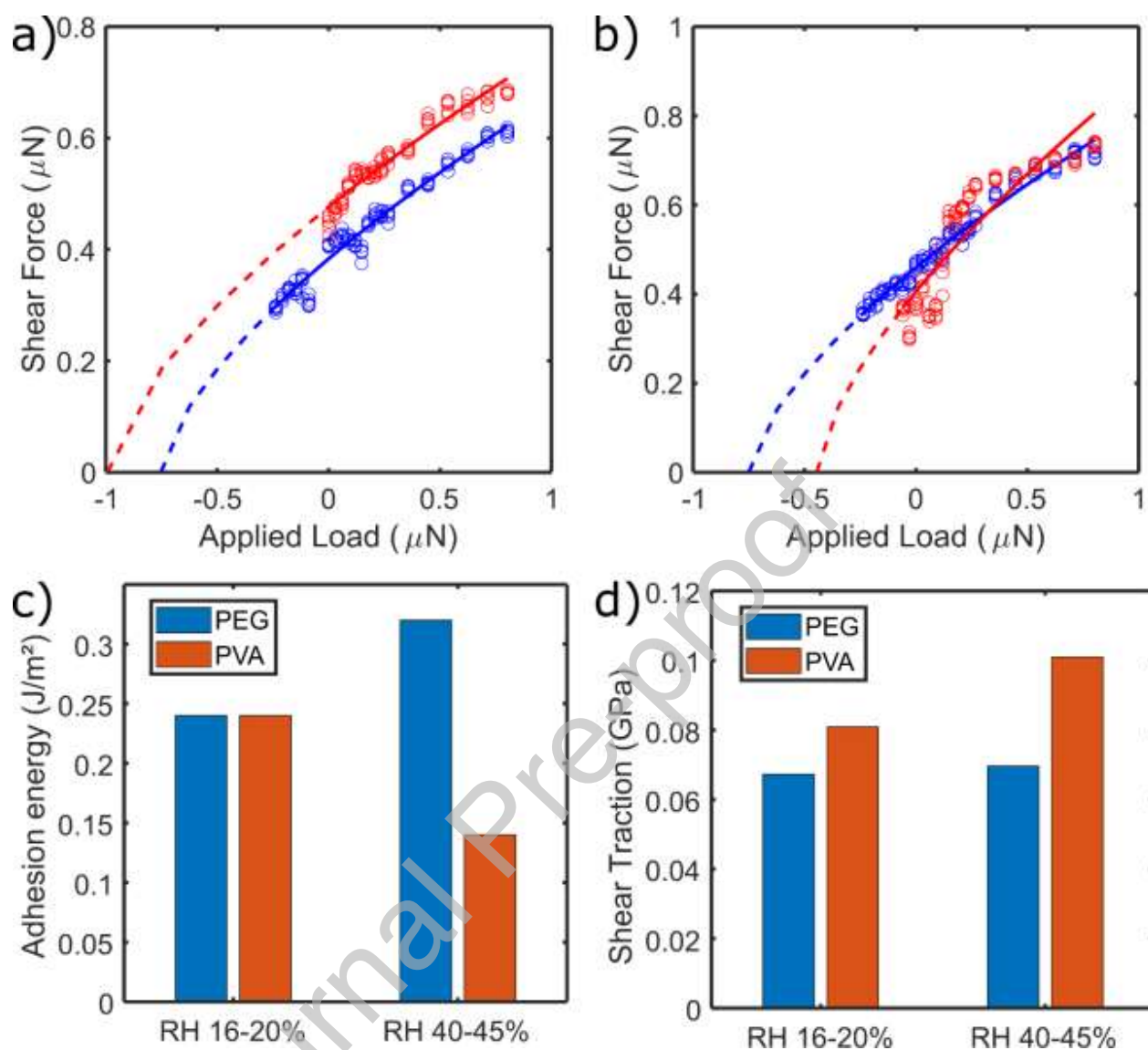


Fig. G.1. Experimental interfacial properties at 16-20% and 40-45% relative humidity.

Reference

- Ackbarow, T., X. Chen, S. Keten and M. J. Buehler (2007). "Hierarchies, multiple energy barriers, and robustness govern the fracture mechanics of α -helical and β -sheet protein domains." *Proc. Natl. Acad. Sci.* **104**(42): 16410-16415.
- Benedetti, I., H. Nguyen, R. A. Soler-Crespo, W. Gao, L. Mao, A. Ghasemi, J. Wen, S. Nguyen and H. D. Espinosa (2018). "Formulation and validation of a reduced order model of 2D materials exhibiting a two-phase microstructure as applied to graphene oxide." *J. Mech. Phys. Solids* **112**: 66-88.
- Borini, S., R. White, D. Wei, M. Astley, S. Haque, E. Spigone, N. Harris, J. Kivioja and T. Ryhanen (2013). "Ultrafast graphene oxide humidity sensors." *ACS Nano* **7**(12): 11166-11173.
- Cannara, R. J., M. Eglin and R. W. Carpick (2006). "Lateral force calibration in atomic force microscopy: A new lateral force calibration method and general guidelines for optimization." *Rev. Sci. Instrum.* **77**(5): 053701.
- Carpick, R. W., D. F. Ogletree and M. Salmeron (1999). "A General Equation for Fitting Contact Area and Friction vs Load Measurements." *J. Colloid Interface Sci.* **211**(2): 395-400.
- Compton, O. C., S. W. Cranford, K. W. Putz, Z. An, L. C. Brinson, M. J. Buehler and S. T. Nguyen (2012). "Tuning the Mechanical Properties of Graphene Oxide Paper and Its Associated Polymer Nanocomposites by Controlling Cooperative Intersheet Hydrogen Bonding." *ACS Nano* **6**(3): 2008-2019.
- Derjaguin, B. V., V. M. Muller and Y. P. Toporov (1975). "Effect of contact deformations on the adhesion of particles." *J. Colloid Interface Sci.* **53**(2): 314-326.
- Dikin, D. A., S. Stankovich, E. J. Zimney, R. D. Piner, G. H. Dommett, G. Evmenenko, S. T. Nguyen and R. S. Ruoff (2007). "Preparation and characterization of graphene oxide paper." *Nature* **448**(7152): 457-460.
- Erickson, K., R. Erni, Z. Lee, N. Alem, W. Gannett and A. Zettl (2010). "Determination of the Local Chemical Structure of Graphene Oxide and Reduced Graphene Oxide." *Adv. Mater.* **22**(40): 4467-4472.
- Fonseca, A. F., T. Liang, D. Zhang, K. Choudhary and S. B. Sinnott (2016). "Probing the accuracy of reactive and non-reactive force fields to describe physical and chemical properties of graphene-oxide." *Comp. Mater. Sci.* **114**: 236-243.
- Hu, M. and B. Mi (2013). "Enabling graphene oxide nanosheets as water separation membranes." *Environ. Sci. Technol.* **47**(8): 3715-3723.
- Humphrey, W., A. Dalke and K. Schulten (1996). "VMD: Visual molecular dynamics." *J. Mol. Graphics* **14**(1): 33-38.
- Johnson, K. L., K. Kendall, A. D. Roberts and D. Tabor (1971). "Surface energy and the contact of elastic solids." *Proc. R. Soc. A* **324**(1558): 301-313.
- Luzar, A. and D. Chandler (1996). "Hydrogen-bond kinetics in liquid water." *Nature* **379**(6560): 55-57.
- Mannoor, M. S., H. Tao, J. D. Clayton, A. Sengupta, D. L. Kaplan, R. R. Naik, N. Verma, F. G. Omenetto and M. C. McAlpine (2012). "Graphene-based wireless bacteria detection on tooth enamel." *Nat. Commun.* **3**: 763.
- Medhekar, N. V., A. Ramasubramaniam, R. S. Ruoff and V. B. Shenoy (2010). "Hydrogen Bond Networks in Graphene Oxide Composite Paper: Structure and Mechanical Properties." *ACS Nano* **4**(4): 2300-2306.
- Owuor, P. S., C. F. Woellner, T. Li, S. Vinod, S. Ozden, S. Kosolwattana, S. Bhowmick, L. X. Duy, R. V. Salvatierra, B. Wei, S. A. S. Asif, J. M. Tour, R. Vajtai, J. Lou, D. S. Galvao, C. S. Tiwary

- and P. M. Ajayan (2017). "High Toughness in Ultralow Density Graphene Oxide Foam." *Adv. Mater. Interfaces* **4**(10): 1700030.
- Plimpton, S. (1995). "Fast Parallel Algorithms for Short-Range Molecular-Dynamics." *J. Comput. Phys.* **117**(1): 1-19.
- Putz, K. W., O. C. Compton, M. J. Palmeri, S. T. Nguyen and L. C. Brinson (2010). "High-Nanofiller-Content Graphene Oxide-Polymer Nanocomposites via Vacuum-Assisted Self-Assembly." *Adv. Funct. Mater.* **20**(19): 3322-3329.
- Rabinovich, Y. I., J. J. Adler, A. Ata, R. K. Singh and B. M. Moudgil (2000). "Adhesion between Nanoscale Rough Surfaces: I. Role of Asperity Geometry." *J. Colloid Interface Sci.* **232**(1): 10-16.
- Sinko, R. and S. Keten (2015). "Traction-separation laws and stick-slip shear phenomenon of interfaces between cellulose nanocrystals." *J. Mech. Phys. Solids* **78**: 526-539.
- Soler-Crespo, R. A., W. Gao, L. Mao, H. T. Nguyen, M. R. Roenbeck, J. T. Paci, J. Huang, S. T. Nguyen and H. D. Espinosa (2018). "The role of water in mediating interfacial adhesion and shear strength in graphene oxide." *ACS Nano* **12**(6): 6089-6099.
- Soler-Crespo, R. A., W. Gao, P. Xiao, X. Wei, J. T. Paci, G. Henkelman and H. D. Espinosa (2016). "Engineering the Mechanical Properties of Monolayer Graphene Oxide at the Atomic Level." *J. Phys. Chem. Lett.* **7**(14): 2702-2707.
- Soler-Crespo, R. A., L. Mao, J. Wen, H. T. Nguyen, X. Zhang, X. Wei, J. Huang, S. T. Nguyen and H. D. Espinosa (2019). "Atomically thin polymer layer enhances toughness of graphene oxide monolayers." *Matter* **1**(2): 369-388.
- Song, P., Z. Xu, Y. Wu, Q. Cheng, Q. Guo and H. Wang (2017). "Super-tough artificial nacre based on graphene oxide via synergistic interface interactions of π - π stacking and hydrogen bonding." *Carbon* **111**: 807-812.
- Stukowski, A. (2009). "Visualization and analysis of atomistic simulation data with OVITO—the Open Visualization Tool." *Modell. Simul. Mater. Sci. Eng.* **18**(1): 015012.
- Vanommeslaeghe, K., E. Hatcher, C. Acharya, S. Kundu, S. Zhong, J. Shim, E. Darian, O. Guvench, P. Lopes, I. Vorobyov and A. D. MacKerell (2010). "CHARMM General Force Field: A Force Field for Drug-Like Molecules Compatible with the CHARMM All-Atom Additive Biological Force Fields." *J. Comput. Chem.* **31**(4): 671-690.
- Vanommeslaeghe, K., E. P. Raman and A. D. MacKerell (2012). "Automation of the CHARMM General Force Field (CGenFF) II: Assignment of Bonded Parameters and Partial Atomic Charges." *J. Chem. Inf. Model.* **52**(12): 3155-3168.
- Wan, S., H. Hu, J. Peng, Y. Li, Y. Fan, L. Jiang and Q. Cheng (2016). "Nacre-inspired integrated strong and tough reduced graphene oxide-poly(acrylic acid) nanocomposites." *Nanoscale* **8**(10): 5649-5656.
- Wan, S., J. Peng, L. Jiang and Q. Cheng (2016). "Bioinspired Graphene-Based Nanocomposites and Their Application in Flexible Energy Devices." *Adv. Mater.* **28**(36): 7862-7898.
- Wan, S., J. Peng, Y. Li, H. Hu, L. Jiang and Q. Cheng (2015). "Use of Synergistic Interactions to Fabricate Strong, Tough, and Conductive Artificial Nacre Based on Graphene Oxide and Chitosan." *ACS Nano* **9**(10): 9830-9836.
- Wang, Y., R. Ma, K. Hu, S. Kim, G. Fang, Z. Shao and V. V. Tsukruk (2016). "Dramatic Enhancement of Graphene Oxide/Silk Nanocomposite Membranes: Increasing Toughness, Strength, and Young's modulus via Annealing of Interfacial Structures." *ACS Appl. Mater. Interfaces* **8**(37): 24962-24973.
- Wei, X., L. Mao, R. A. Soler-Crespo, J. T. Paci, J. Huang, S. T. Nguyen and H. D. Espinosa (2015). "Plasticity and ductility in graphene oxide through a mechanochemically induced damage tolerance mechanism." *Nat. Commun.* **6**(1): 8029.

- Xie, W., S. Tadepalli, S. H. Park, A. Kazemi-Moridani, Q. Jiang, S. Singamaneni and J.-H. Lee (2018). "Extreme mechanical behavior of nacre-mimetic graphene-oxide and silk nanocomposites." *Nano Lett.* **18**(2): 987-993.
- Yu, W., X. He, K. Vanommeslaeghe and A. D. MacKerell Jr (2012). "Extension of the CHARMM general force field to sulfonyl-containing compounds and its utility in biomolecular simulations." *J. Comput. Chem.* **33**(31): 2451-2468.
- Zhang, X., H. Nguyen, M. Daly, S. T. Nguyen and H. D. Espinosa (2019). "Nanoscale toughening of ultrathin graphene oxide-polymer composites: Mechanochemical insights into hydrogen-bonding/van der Waals interactions, polymer chain alignment, and steric parameters." *Nanoscale* **11**(25): 12305-12316.

Declaration of interests

The authors declare that they have no known competing financial interests or personal relationships that could have appeared to influence the work reported in this paper.